Final Report

submitted to

NATIONAL AERONAUTICS AND SPACE ADMINISTRATION
GEORGE C. MARSHALL SPACE FLIGHT CENTER, ALABAMA 35812

October 20, 1994

for Contract NAS8 - 38609

Delivery Order 99

entitled

# Acoustic Method of Damage Sensing in Composite Materials

by

Gary L. Workman Ph.D.
Principal Investigator

and

James Walker
Graduate Student

Matthew Lansing
Research Associate

Materials Processing Laboratory
Center for Automation & Robotics
University of Alabama in Huntsville
Huntsville, Alabama 35899

TABLE OF CONTENTS

*General Introduction*

The technological improvements in many of today's aerospace structures are primarily due to new and advanced materials and processes. As requirements increase for these improved materials, so does the need to determine structural integrity of the components used in these systems. Both nondestructive evaluation and materials characterization of critical aerospace structures are areas which continually need to be considered in the implementation of new materials into aerospace systems. For this reason, research efforts in NDE must keep pace with the developement of new materials and processes. There are a number of NDE techniques which can provide useful information about flaw size and location; such as ultrasonics, eddy current, and radiography. However, these techniques usually require a significant flaw size to exist so that a minimum threshold is reached. Other technique which are currently available for monitoring composite materials include acoustic emission (AE) testing, acusto-ultrasonics (AU), and shearography.

Since AE does not depend upon flaw size to characterize a flaw, it can be extremely sensitive. Acoustic emission testing of aerospace structures has the potential to 'proof-test' critical structures without impairing the ability of the structure to perform its normal role in service. A major application of this technology to is the hyrostatic proof testing of composite structures. AE sensitivity is primarly dependent upon both the sensors used and the characteristics of the test material. Ultrasonic wave propagation affects the time domain and waveform characteristics and energy of broken bonds affects signal strength. Variations in these parameters affect the AE sensitivity and flaw interpretation.

AU principles are the same as AE, with the exception that instead of listening to cracks propagating, one inputs an ultrasonic pulse (or stress wave) and monitors the effect of the structure on that waveform. This methodology, in parallel with the shearography work, has been the primary activity worked in this pahse of the damage assessment program. Correspondingly, this report is divided into the two sections, presenting the results of the two methods separately. It is hopeful that once the overall damage assessment program runs full course, a synopsis of all the results can be integrated into one analysis.

ACOUSTIC METHODS
TABLE OF CONTENTS

## 1.0 Introduction

An acousto-ultrasonic (AU) nondestructive evaluation (NDE) system is under development for assessing the extent of impact damage to filament wound composite pressure vessels. The current AU system utilizes a 500 kHz pulser and broadband (100 to 1000 kHz) receiver to record the acoustic signature of a structure. Eleven graphite/epoxy bottles have been AU mapped with the current AU system to determine its ability to measure the extent of impact damage in composite structures. Measurements were taken along and perpendicular to the hoop fiber direction for these eleven bottles. The power spectrum and resulting spectral energy were tabulated for each acoustic signal. The energy was then plotted versus bottle location as a first test of the AU system to quantify the extent of impact damage. This report describes the results of the preliminary study and will address;

1. The experimental system used to collect AU data
2. The analysis procedure
3. Preliminary results from the current AU system
4. Limitations and improvements.

## 2.0 Theoretical Basis

Acousto-Ultrasonics serve as a NDE tool by combining the technologies of Acoustic Emission (AE) and ultrasonics. The AU system records the response of a structure to an ultrasonic pulse, similar to that of through-transmission ultrasonics. A pulser driving an ultrasonic transducer is configured to inject a single strain wave (acoustic signal) into the structure. The signal passes through the structure and is transformed by the complex interactions of itself with the material volume and then is received by an AE transducer. The parameters of the recorded acoustic signal, or event, then carries with it a fingerprint of the integrity and quality of the material between the pulser and receiver. By analyzing the AE parameters of the signal along with the frequency (power) spectrum a correlation with the material properties and overall strength of the structure can be deduced.

A stress wave factor (SWF) is defined as a measure of the received signals strength. The stress wave factor can take on many forms ranging from a simple amplitude measurement to an integration of the power spectrum. Researchers have devised many different ways to calculate the SWF for specific structural cases. For this work the energy associated with two specific frequency bands of the power spectrum was chosen to represent the SWF. The two intervals selected, range from 25 to 375 kHz and 375 to 700 kHz, based on an apparent grouping in the power spectrum curves (Figure 1).

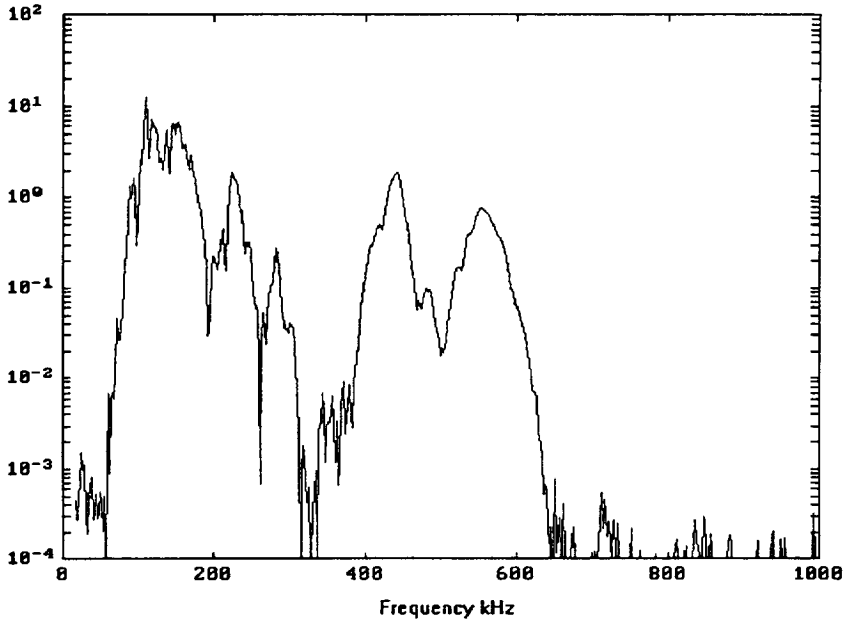


**Figure 1. Power spectrum.**

The basic requirement for a valid SWF is that it provide an indication as to the structural quality of a pressure vessel before an impact as well as be directly related to the amount of damage attained from an impact. The SWF will also be related to manufacturing variations such as voids in the resin or misaligned fibers and experimental variables including contact pressure and degree of sensor coupling.

By mapping the SWF for the entire bottle, regions of poor quality will be located before impact. After impact the SWF map should change in the damaged zone so that a measure of the extent of damage can be made. Depending upon the severity of the damage attained at impact the SWF may or may not be lower than the lowest value found before impact. The lowest region should be where the vessel ultimately fails.

## 3.0 Experimental Approach

An ultrasonic pulser and a standard AE recording system are combined to form the AU system. The heart of the AU system is the Physical Acoustics Corporation (PAC) SPARTAN AE system which serves to measure and record the AE signal parameters as well as store the actual event on its TRA board from a PAC model W4I receiver. A Harisonic 500 kHz ultrasonic transducer driven by a Panametrics model 5055PR pulser is used as the transmitter. The receiver and pulser are coupled to the surface using Sonotrace ultrasonic couplant. The pulser is triggered by a pulse from a Wavetek Pulse/Function generator so as to generate a single waveform. The AU system is shown in Figure 2.

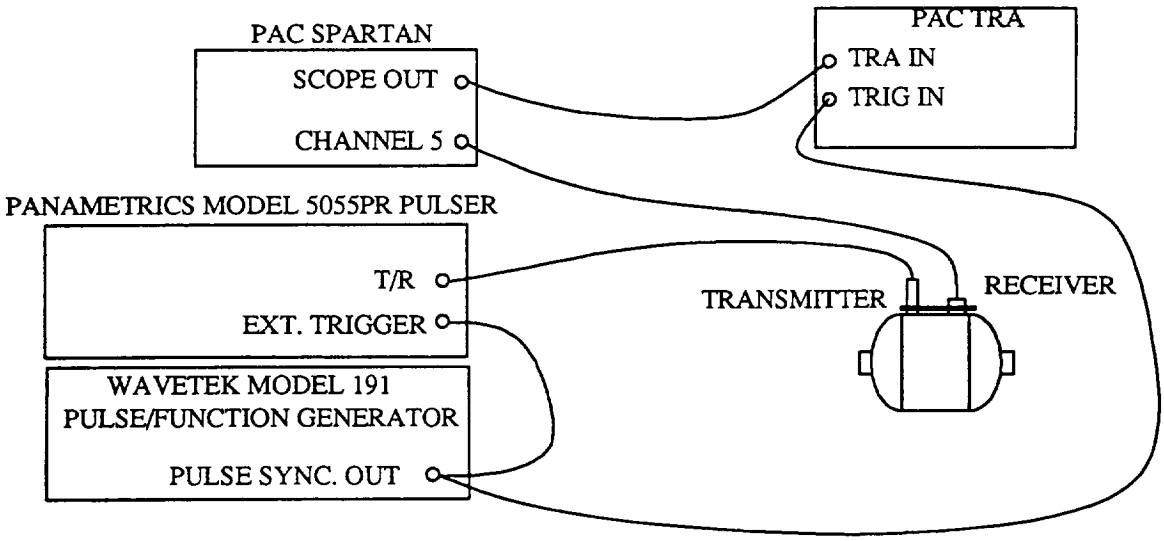


**Figure 2. Acousto-Ultrasonic system schematic.**

Transducer spacing and contact pressure is often a problem associated with AU measurements. To overcome these problems two simple holders were constructed from 1/4 inch thick Plexiglas providing a means to position the transducers relative to each other and press them to the structure. A simple flat holder (Figure 3) was used for making measurements perpendicular to the hoop direction while a hinged version (Figure 4) was constructed for making measurements around the hoop direction of the bottle. A two pound steel weight is bonded to both holders to provide the constant contact pressure. The holders were designed to maintain a 1.5 inch sensor spacing.

## 4.0 Signal Analysis

The recorded AU signal was first converted to ASCII format through the PAC program TRA2DAD.EXE. This program generates a data file consisting of a seven line header followed by a sequential string of values representing the signal's digitized amplitudes. For this work the sampling rate was set at 16 MHz for a total of 8192 points. The ASCII data file is then run through the BASIC program "TRA2MLAB.BAS" which eliminates the header and puts the file into MATLAB format. The program "ENGYDATA.M" is then executed by MATLAB to compute the energy for the two frequency bands. Finally, the resulting energy table from MATLAB is processed by another BASIC program "OUTPUT.BAS" which computes the average of the readings for one position and orders the data into a convenient form. The programs just described can be found in the Appendix of this report.

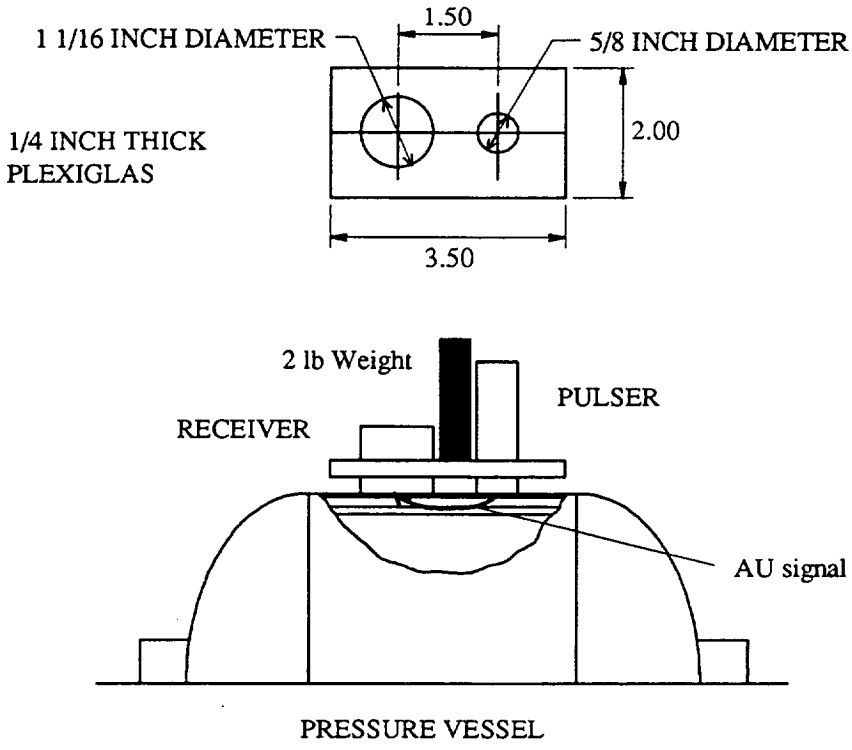


**Figure 3. Flat transducer holder.**

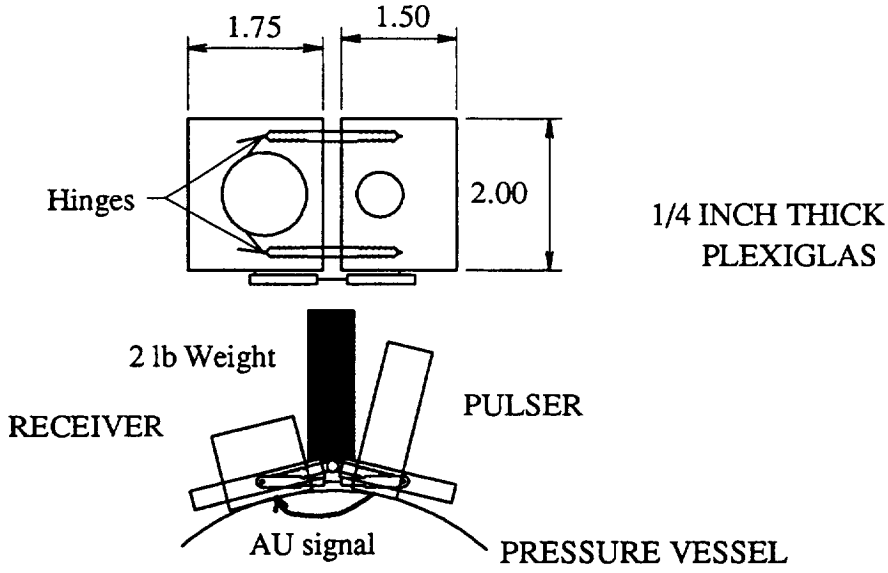


**Figure 4. Hinged transducer holder.**

## 5.0 RESULTS

A sample of the energies and position versus energy plots for the AU data taken perpendicular to the hoop direction is provided in Figure 6 and Table 1 and 2. The data in the energy tables is ordered from readings taken from the bottom to the top of the bottle (Figure 5). At each circumference location (Lc.) three readings were taken and averaged to help reduce the effects of local surface roughness and sensor couplant variations. The plot of position versus energy show only the averaged values for each location.

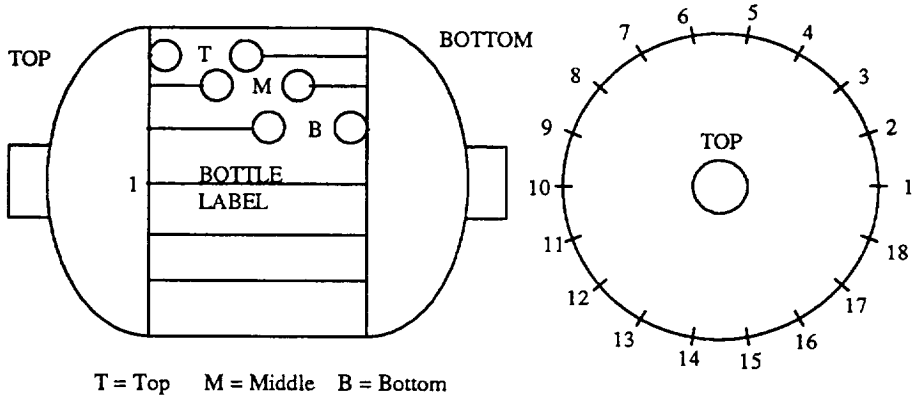


**Figure 5. Bottle position and sensor and sensor locations for transverse measurements.**

A sample of the data taken along the hoop direction is provided in Figure 8 and Table 3. The AU data was taken using the hinged transducer holder from top to bottom along the length of the bottle in the hoop direction. The data was taken at seven positions spaced 1/2 inch apart through the impact point (Figure 7). Again three measurements were taken at each location and averaged.

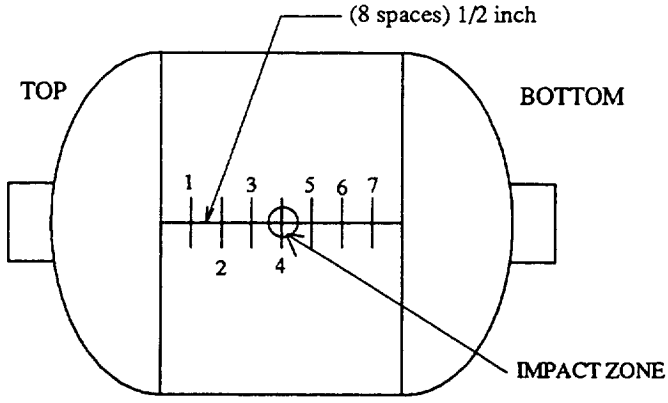


**Figure 7. Hoop data transducer positions.**

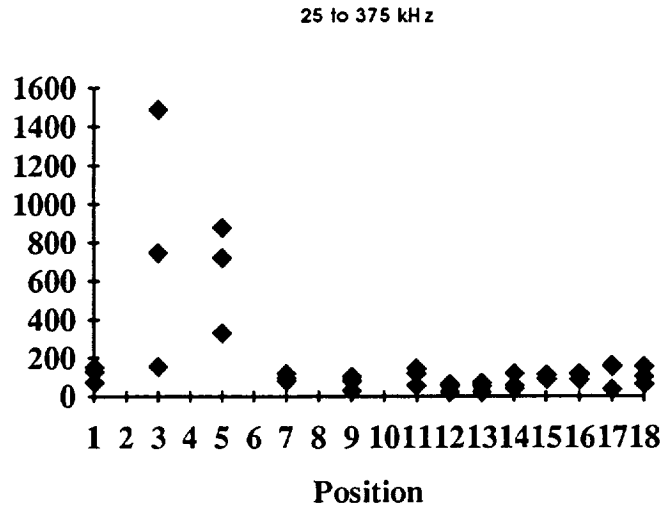


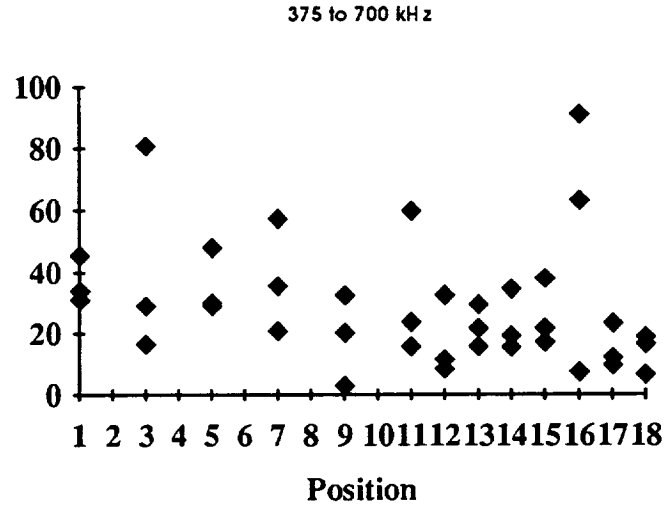


Figure 6. Energy versus position for bottle A013-014.

| Lc. | Energy 25 kHz to 375 kHz | | | Avg. |
|---|---|---|---|---|
| 1B | 76.95071 | 201.7045 | 116.9022 | 131.8525 |
| 1M | 177.36 | 151.6672 | 119.4325 | 149.4865 |
| 1T | 63.57466 | 88.52828 | 68.7368 | 73.61325 |
| 3B | 88.0383 | 186.1263 | 198.9304 | 157.6983 |
| 3M | 1312.56 | 1534.095 | 1621.043 | 1489.233 |
| 3T | 629.1249 | 1112.008 | 506.5085 | 749.2137 |
| 5B | 509.8815 | 377.9018 | 108.1348 | 331.9727 |
| 5M | 955.2031 | 751.8484 | 461.0319 | 722.6945 |
| 5T | 1363.515 | 611.244 | 665.423 | 880.0607 |
| 7B | 81.34312 | 41.99632 | 171.5611 | 98.30019 |
| 7M | 74.87201 | 68.69031 | 205.7554 | 116.4393 |
| 7T | 58.11505 | 95.11954 | 86.84006 | 80.02489 |
| 9B | 34.04049 | 27.23174 | 37.78384 | 33.01869 |
| 9M | 68.63525 | 61.58098 | 103.7944 | 78.00356 |
| 9T | 137.7847 | 71.05717 | 89.92639 | 99.58943 |
| 11B | 72.93637 | 29.35582 | 78.48004 | 60.25741 |
| 11M | 136.6818 | 71.16397 | 150.3705 | 119.4054 |
| 11T | 201.3761 | 134.1547 | 95.64552 | 143.7254 |
| 12B | 47.32289 | 68.1264 | 45.00477 | 53.48469 |
| 12M | 104.4929 | 56.32137 | 28.80478 | 63.20635 |
| 12T | 42.44805 | 24.94477 | 13.36436 | 26.91906 |
| 13B | 29.22311 | 16.64987 | 30.25349 | 25.37549 |
| 13M | 38.86938 | 61.30444 | 66.90422 | 55.69268 |
| 13T | 65.5771 | 74.97065 | 75.27665 | 71.94147 |
| 14B | 44.52494 | 53.80404 | 33.68908 | 44.00602 |
| 14M | 141.0434 | 137.3906 | 68.86568 | 115.7666 |
| 14T | 60.31449 | 73.07755 | 37.13707 | 56.84304 |
| 15B | 86.12859 | 107.7392 | 71.81441 | 88.56073 |
| 15M | 161.0271 | 93.08582 | 91.45146 | 115.1881 |
| 15T | 109.4742 | 76.35391 | 88.97192 | 91.60002 |
| 16B | 99.2156 | 93.85016 | 69.75635 | 87.60737 |
| 16M | 166.7669 | 122.1736 | 73.42812 | 120.7895 |
| 16T | 117.5708 | 148.567 | 80.03483 | 115.3909 |
| 17B | 45.05859 | 55.49792 | 14.16126 | 38.23925 |
| 17M | 216.5525 | 124.82 | 137.8694 | 159.7473 |
| 17T | 198.5833 | 142.0562 | 122.4768 | 154.3721 |
| 18B | 90.19291 | 56.82689 | 47.16758 | 64.72913 |
| 18M | 164.6483 | 188.4032 | 108.241 | 153.7642 |
| 18T | 121.9876 | 124.7275 | 56.60427 | 101.1065 |

**Table 1. Energy table (25-375 kHz) for bottle A013-014.**

| Lc. | Energy 375 kHz to 700 kHz | | | Avg. |
|---|---|---|---|---|
| 1B | 37.85745 | 44.425 | 54.83997 | 45.70747 |
| 1M | 33.80395 | 26.60864 | 32.86417 | 31.09225 |
| 1T | 22.29725 | 48.494 | 31.35759 | 34.04961 |
| 3B | 9.81923 | 21.77394 | 18.44153 | 16.67823 |
| 3M | 79.65441 | 84.86322 | 77.95669 | 80.82478 |
| 3T | 41.18616 | 30.29874 | 15.79074 | 29.09188 |
| 5B | 36.94177 | 27.97573 | 22.86202 | 29.25984 |
| 5M | 41.71772 | 26.70184 | 22.3021 | 30.24055 |
| 5T | 54.24715 | 37.20598 | 53.30939 | 48.25417 |
| 7B | 24.89395 | 24.04889 | 14.10718 | 21.01667 |
| 7M | 32.60492 | 30.72009 | 43.87755 | 35.73418 |
| 7T | 82.29337 | 46.07584 | 43.86423 | 57.41115 |
| 9B | 13.1073 | 23.51475 | 61.49747 | 32.7065 |
| 9M | 1.608922 | 1.889013 | 4.975831 | 2.824589 |
| 9T | 15.90941 | 18.52054 | 26.17822 | 20.20272 |
| 11B | 12.21831 | 12.37868 | 46.6958 | 23.76426 |
| 11M | 21.12417 | 12.67794 | 13.79656 | 15.86622 |
| 11T | 66.57324 | 60.13491 | 52.94274 | 59.88363 |
| 12B | 52.59336 | 28.94081 | 15.71363 | 32.41593 |
| 12M | 10.02702 | 9.491334 | 6.12777 | 8.548708 |
| 12T | 12.45468 | 8.955417 | 12.86144 | 11.42385 |
| 13B | 30.22991 | 20.29663 | 38.03727 | 29.52127 |
| 13M | 16.96794 | 15.44838 | 14.95261 | 15.78964 |
| 13T | 33.80959 | 16.58268 | 14.20264 | 21.53164 |
| 14B | 12.05603 | 21.60242 | 13.49345 | 15.7173 |
| 14M | 31.01821 | 26.69358 | 46.57515 | 34.76231 |
| 14T | 19.52214 | 15.91289 | 22.87333 | 19.43612 |
| 15B | 40.9946 | 33.84901 | 39.46914 | 38.10425 |
| 15M | 11.89209 | 21.36076 | 18.49797 | 17.25027 |
| 15T | 23.89145 | 20.36845 | 21.11899 | 21.79296 |
| 16B | 107.9897 | 55.00666 | 26.82556 | 63.27397 |
| 16M | 9.3914 | 8.126588 | 5.1404 | 7.552796 |
| 16T | 109.9818 | 103.2883 | 59.49157 | 90.92056 |
| 17B | 7.344246 | 15.97499 | 12.94868 | 12.0893 |
| 17M | 19.00625 | 22.90672 | 28.71361 | 23.54219 |
| 17T | 6.976822 | 10.40543 | 11.50189 | 9.628047 |
| 18B | 20.69502 | 7.641919 | 21.74108 | 16.69267 |
| 18M | 22.67903 | 15.53958 | 18.27721 | 18.83194 |
| 18T | 5.694066 | 5.021621 | 9.607473 | 6.774387 |

**Table 2. Energy table (375-700 kHz) for bottle A013-014.**

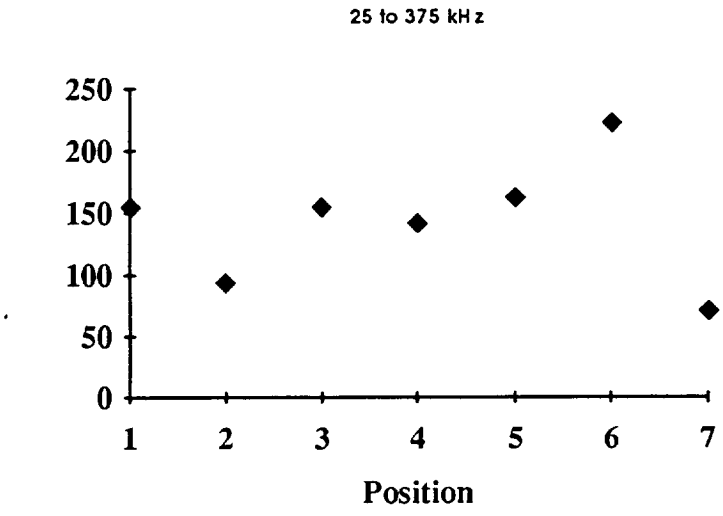


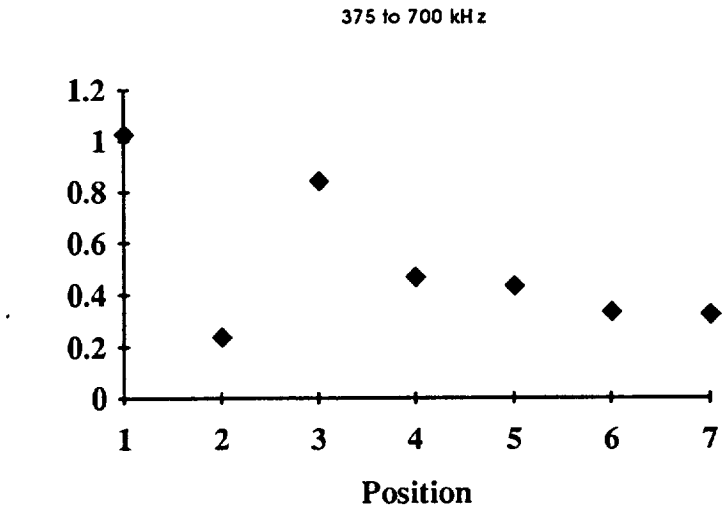


Figure 8. Energy versus position for bottle A013-014.

| | 25 kHz to 375 kHz | | | Avg. |
|---|---|---|---|---|
| 0, 1, 2 | 161.2777 | 152.503 | 148.9198 | 154.2335 |
| 3, 4, 5 | 99.76716 | 100.34 | 82.93896 | 94.34872 |
| 6, 7, 8 | 175.6977 | 152.5769 | 135.5376 | 154.6041 |
| 9, 10, 11 | 137.9272 | 137.1744 | 150.8726 | 141.9914 |
| 12, 13, 14 | 138.3078 | 171.6441 | 175.6549 | 161.869 |
| 15, 16, 17 | 234.7992 | 237.1654 | 196.5073 | 222.824 |
| 18, 19, 20 | 64.91631 | 67.5603 | 80.13531 | 70.87064 |
| | 375 kHz to 700 kHz | | | Avg. |
| 0, 1, 2 | 1.134663 | .9083912 | 1.043809 | 1.028954 |
| 3, 4, 5 | .2097775 | .2972545 | .2083055 | .2384458 |
| 6, 7, 8 | .9983227 | .781202 | .7506411 | .8433886 |
| 9, 10, 11 | .4357781 | .5108677 | .4565105 | .4677188 |
| 12, 13, 14 | .3091225 | .507862 | .4850739 | .4340195 |
| 15, 16, 17 | .3654976 | .2642473 | .3755382 | .3350944 |
| 18, 19, 20 | .2952006 | .314505 | .3680085 | .3259047 |

Table 3. Energy table for bottle A013-014.

## 6.0 Principal Component Approach

In addition to the neural networks, a new concept has been tried, which allows for classification of the acousto-ultrasonic data into more general groupings than neural nets by themselves. We have had very success in earlier research in determining levels and identities of contaminants on solid rocket motor components using Principal Component Analysis (PCA) and related techniques such as Principal Component Regression (PCR) and Partial Least Squares (PLS). The latter two techniques require that a y component exist in the dataset, which was normally an associated measurement. For instance in the solid rocket motor work, y could be a temperature, humidity or OSEE measurement performed in conjunction with the spectral data taken at the same time. The x data was always a spectrum taken of the surface materials. These techniques worked well in those cases and provided both classification and quantitative indication of particular chmeistries.

For the present work, a sample case was pursued by taking the energies for the high frequency components of the AU data obtained for the impacted bottles and performing a PCA on them using Unscrambler II® software. This is the same software used in the spectral work described above. The following charts were obtained for the loadings and scores in the analysis. Note that the loadings of the principal components are the significant data obtained from the consolidated dataset and the loadings represent the relative influence of each of the measurement sets on principal component or factor. For example, one would expect the loadings for the impacted bottle to show the primary factors(s) with loadings which have a siginificantly different energy around the impacted

zone versus the areas away from the impacted zone. The corresponding scores then represent the influence each bottle has on that particular loading. For example, differences in measurements due to resin type, impactor type, or other features may show up in the different factors and be identified through the scores.

| Bottle | P1 | P2 | P3 | P4 | P5 | P6 | P7 |
|---|---|---|---|---|---|---|---|
| a013a | 1.1347 | 0.2098 | 0.9983 | 0.4358 | 0.3091 | 0.3655 | 0.2952 |
| | 0.9084 | 0.2973 | 0.7812 | 0.5109 | 0.5079 | 0.2642 | 0.3145 |
| | 1.0438 | 0.2083 | 0.7506 | 0.4565 | 0.4851 | 0.3755 | 0.3680 |
| a017a | 0.0857 | 0.2097 | 0.4618 | 0.4596 | 0.7346 | 0.7124 | 0.0962 |
| | 0.2419 | 0.5013 | 0.3680 | 0.3617 | 1.3101 | 0.3697 | 0.0853 |
| | 0.5178 | 0.8392 | 0.1330 | 0.2956 | 0.9015 | 0.5407 | 0.0989 |
| a029a | 0.2318 | 0.1142 | 0.4969 | 1.1907 | 0.1519 | 0.3067 | 0.3496 |
| | 0.2257 | 0.1523 | 0.9344 | 3.1600 | 0.1604 | 0.2474 | 0.1570 |
| | 0.2555 | 0.1689 | 0.8775 | 1.2574 | 0.2811 | 0.1457 | 0.1720 |
| a047a | 0.5898 | 0.6745 | 0.5161 | 6.7192 | 0.1337 | 0.1096 | 0.0268 |
| | 0.5468 | 1.0493 | 0.8295 | 0.9756 | 0.1112 | 0.0917 | 0.0110 |
| | 0.4051 | 0.7481 | 0.5019 | 3.9532 | 0.0856 | 0.0739 | 0.0166 |
| a069a | 1.1149 | 2.6279 | 6.6797 | 42.3428 | 103.7719 | 18.8755 | 2.1692 |
| | 1.2631 | 1.6219 | 4.1887 | 52.9087 | 182.9021 | 13.4737 | 1.5118 |
| | 1.2317 | 1.7374 | 13.3643 | 26.3644 | 68.1587 | 15.3910 | 1.4962 |
| c077a | 1.5381 | 6.2067 | 24.1483 | 20.4088 | 32.9764 | 37.6826 | 3.2953 |
| | 1.5171 | 3.6426 | 72.1261 | 34.4718 | 24.8147 | 38.1574 | 2.7139 |
| | 2.3034 | 3.1888 | 45.7086 | 47.5739 | 44.0305 | 42.3379 | 3.3525 |
| c093a | 0.1826 | 0.0885 | 0.2265 | 0.3198 | 0.5119 | 0.3442 | 0.5019 |
| | 0.0974 | 0.0804 | 0.2107 | 0.2230 | 0.4047 | 0.2841 | 0.4364 |
| | 0.1278 | 0.1250 | 0.2615 | 0.1249 | 0.3534 | 0.2161 | 0.5429 |
| c117a | 3.2936 | 2.9560 | 0.1778 | 11.4225 | 61.1698 | 1.3105 | 0.0301 |
| | 4.6419 | 1.7096 | 0.3002 | 18.5803 | 66.0650 | 1.4522 | 0.0415 |
| | 4.5153 | 2.1430 | 0.3541 | 18.3119 | 53.5003 | 0.7931 | 0.0326 |
| c131a | 2.7839 | 5.5898 | 3.2110 | 0.1825 | 8.6881 | 0.8138 | 0.5118 |
| | 3.0474 | 7.4177 | 3.0553 | 0.2462 | 5.3503 | 0.7440 | 0.3557 |
| | 3.0229 | 5.0650 | 2.8961 | 0.2463 | 5.3285 | 0.7336 | 0.2619 |
| c141a | 4.4313 | 0.4032 | 0.9845 | 40.4508 | 29.5970 | 0.3389 | 0.3213 |
| | 2.1333 | 0.3307 | 0.6758 | 29.7921 | 25.7492 | 0.1850 | 0.1915 |
| | 2.8188 | 0.3525 | 0.4119 | 77.3625 | 19.8353 | 0.3317 | 0.1832 |
| c155a | 9.0353 | 5.4956 | 3.0527 | 3.1847 | 0.0866 | 0.1606 | 0.2145 |
| | 8.5959 | 5.5316 | 3.0277 | 1.5076 | 1.0880 | 0.2253 | 0.2063 |
| | 8.4978 | 5.7104 | 3.2517 | 1.5375 | 0.9438 | 0.3204 | 0.2453 |

The data contains three AU measurements made across each bottle across the impacted zone. P! through P7 represent these seven positions. A graph of this dataset is shown in figure 9 on the next page.

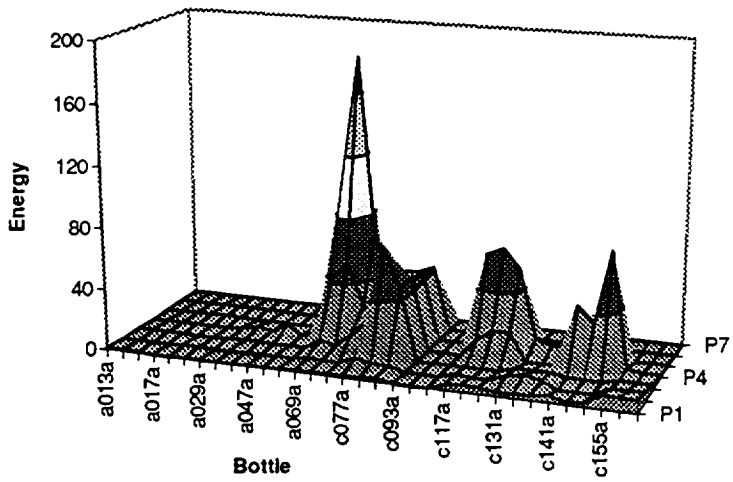


**Figure 8.** 3-D plot of the energy data from Table 4.

It is important to note from figure 8 that the data set contains very large energies for bottles a069 and c077 relative to the others. These values may have a greater influence on the loadings and scores than should actually occur and with some care, weighing of the variables may be useful. In the current analysis the following charts shown in figure 10 are obtained for the scores and loading derived from Table 4. These charts represent variations from the mean of the total measurement set and as such, provides information about the differences between the measurements. All three measurements obtained at each position were retained to improve upon the statistics. The loadings for PC1 and PC2 do show large values for the area on either side of the impacted area and represent 60% of the total variation contained in the data. The relative influence of each of these components on the total measurement set are listed in the chart. This PCA was performed using five factors; however, PC5 is not shown because it primarily oscillates around zero and represents only 4 % of the variation in the data (noise).

**Figure 10.** Principal Component Analysis for high frequency hoop measurements.

a. Scores for PC1 (40%)

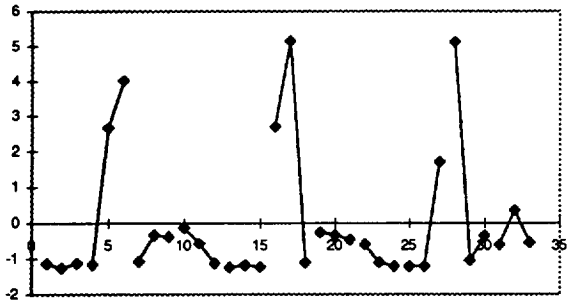

b. Loadings for PC1

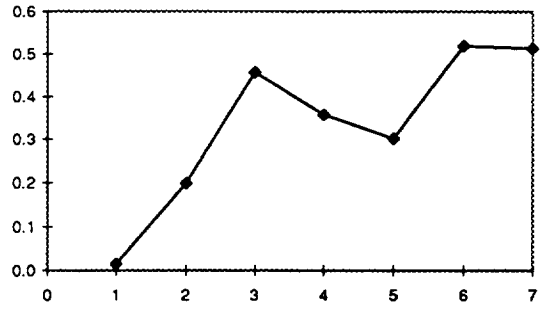

c. Scores for PC2 (20%)

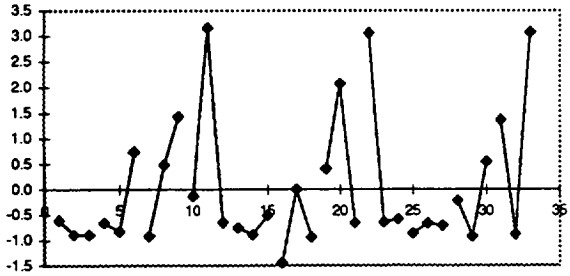

d. Loadings for PC2

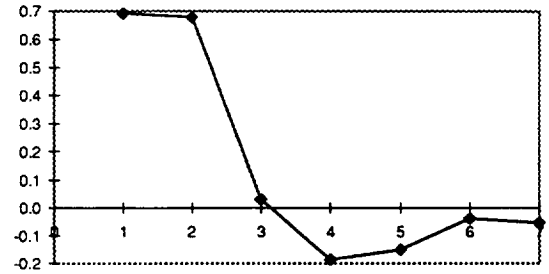

e. Scores for PC3 (20%)

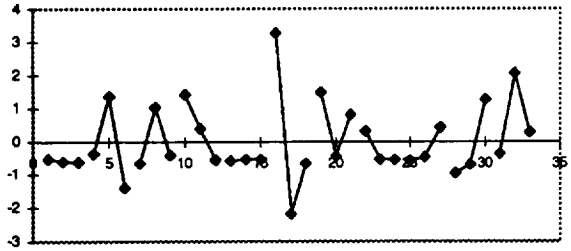

f. Loadings for PC3

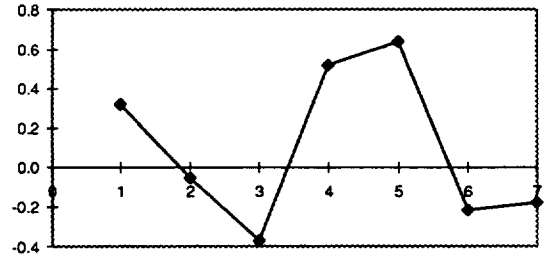

g. Scores for PC4 (9%)

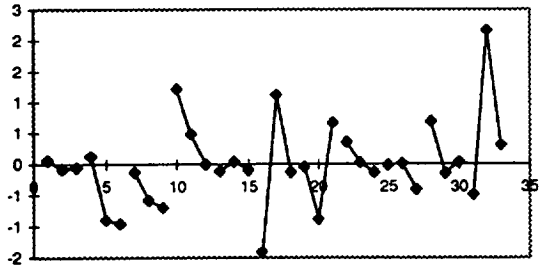

h. Loadings for PC4

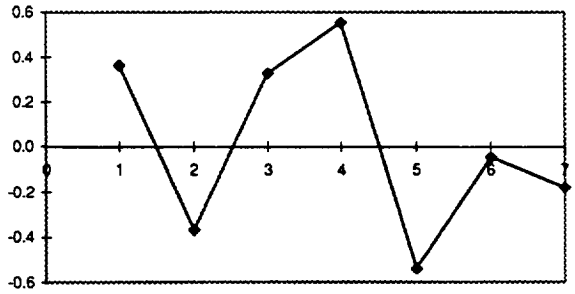

## 7.0 Discussion of Results

The energy bands selected for this preliminary study do not provide an adequate SWF for identifying the impacted regions of the pressure vessels. There were two major sources for the inability of the current system to detect the flawed regions. First, a high degree of surface roughness and curvature combined with a large sensor contact area lead to poor couplant repeatability. The individual values used to compute the averages produced variations greater than 100% in some cases.

Wave guides were constructed from brass and Plexiglas to reduce the footprint of the transducers in an attempt to help reduce the problem of local surface roughness. The combined attenuation of the wave guides and the bottles reduced the already weak AU signal to an impractical level though, such that the background noise dominated the power spectrum. Figure 9 illustrates the wave guides that were constructed for the study.

The second reason that the system was not able to detect the damage zone was that the AU signal had to pass through a "filtered" channel board of the AE system before it could be stored by the TRA system. This meant that the 100 to 300 kHz bandpass filter located on the channel board would block some if not all of the high frequency information of the AU signal. Since the signal was already weak due to the attenuation of the pressure vessel, very little of the high frequency components were recorded. The damage detection threshold of an AU system is directly related to the frequency of the transmitted signal. A small crack

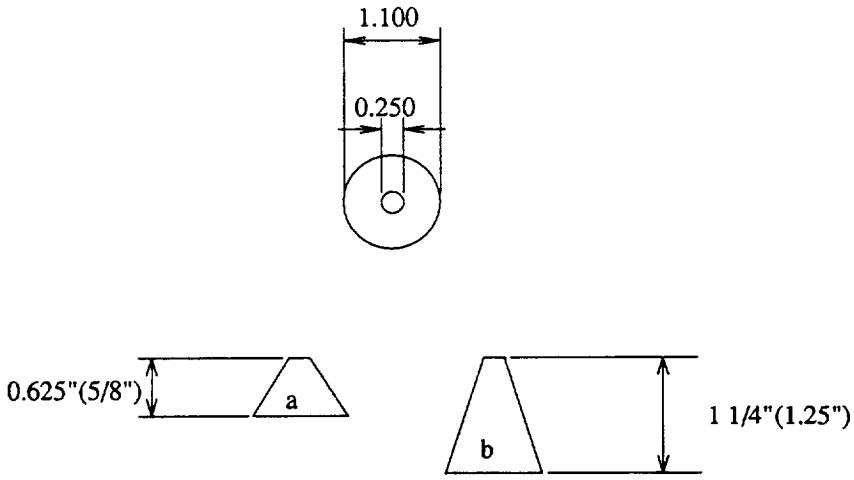


**Figure 11. Wave guides.**

or discontinuity acts as a low pass filter, blocking high frequency components of the signal.

The lower frequency components will pass through a damaged region with little or no effect to its attenuation while higher frequencies will be blocked by the damage. Therefor, since what is being measured by an AU system is the variation in the signals characteristics

from on location on the structure to another, if the higher frequencies are attenuated by the recording system no variations will be measured. The amount that a signal will be attenuated by the filter can be seen in the amplitude frequency response of the channel board shown in figure 12.

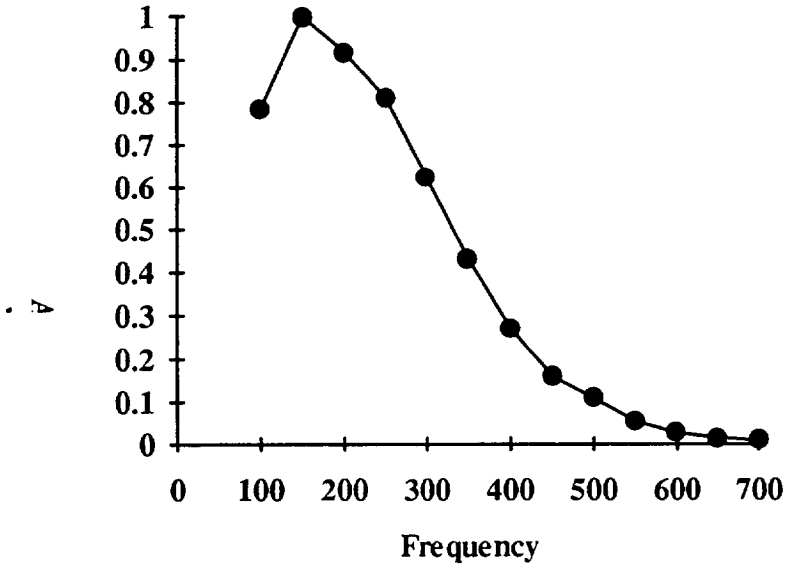


**Figure 10. Amplitude frequency response of SPARTAN system.**

## 8.0 Continuing Research Activities

- A decoupler is being built that will eliminate the need for the SPARTAN AE system as the recorder for the AU system. The decoupler will serve as the power supply for the broadband receiver and will permit the AU signal to pass directly to a PC based ultrasonic board. Since the AU signal will now reside in the PC's memory buffer, MATLAB will be able to directly access the digitized amplitude envelope.

- The current SWF (energy bands) does not provide adequate information for determining the impact status of the pressure vessels. A possible explanation for the failure is that the details of the power spectrum are lost when the energy is computed. To overcome this problem a self-organizing map (SOM) is being developed using neural network modeling software. The SOM will locate any distinguishing characteristics in the power spectrum (if any) through unsupervised training. Once the characteristics of the power spectrum are known a back propagation neural network will be trained to predict the presence of impact damage.

- More work with the PCA will be performed to determine if this approach has any validity in analyzing this type of data. For instance, burst pressures can be used for y's

and extend the analystical techniques to more robust approaches such as PCR and PLS.

## 9.0 APPENDIX

### PROGRAMS USED DURING SIGNAL ANALYSIS

### PROGRAM TRA2MLAB.BAS

```
'
' This program converts a file from the TRA format to a MATLAB format.
' The user should specify the upper limit on the loop before executing
' the program.
'
FOR r = 0 TO 20
 IF r < 10 THEN
  w$ = "ch.00" + LTRIM$(STR$(r))
 END IF
 IF r > 9 AND r < 100 THEN
  w$ = "ch.0" + LTRIM$(STR$(r))
 END IF
 IF r > 99 THEN
  w$ = "ch." + LTRIM$(STR$(r))
 END IF
  ww$ = "ch" + LTRIM$(STR$(r)) + ".m"
  PRINT w$, ww$
  OPEN "i", 1, w$
  OPEN "o", 2, ww$
FOR y = 1 TO 9
LINE INPUT #1, q$
NEXT y
 PRINT #2, "a=[",
 FOR y = 1 TO 8191
  INPUT #1, z
  PRINT #2, z
 NEXT y
  INPUT #1, z
  PRINT #2, z,
  PRINT #2, "];"
CLOSE #1
CLOSE #2
NEXT r
END
```

**PROGRAM ENGYDATA.M**

```
% This program computes the energy content as measured by the area under
% the power spectral density curve for a series of user defined PAC TRA
% files. The input files should first be organized into sequentially
% numbered "m" files befor running this program. The program "TRA2MLAB.BAS"
% can be used to create the "m" files.
!cls
clear                    % Clear all variables.
for k=0:20,              % The range of "m" files.
eval(['ch',int2str(k)]);     % Load the file into MATLAB.
k                        % Indicate the current file number.
a=a*.01;                 % Scale the signal amplitude to volts.
y = fft(a,8192);         % Calculate the FFT for the signal.
Pyy = y.*conj(y)/8192;       % Calculate the power spectral density.
low(k+1)=sum(Pyy(25:192));   % Low energy for file (k+1).
high(k+1)=sum(Pyy(193:359)); % High energy for file (k+1).
end
save low.bas low -ascii      % Save energy data in an ASCII file.
save high.bas high -ascii
```

**PROGRAM OUTPUT.BAS**

```
' This program is used to organize the energy files from MATLAB.
' The input files "low.bas" and "high.bas" are created in MATLAB for a given
' TRA file. The user needs to supply an output filename for files 3 and 4
' and the upper limit on the loop.
OPEN "i", 1, "low.bas"
OPEN "i", 2, "high.bas"
OPEN "o", 3, "a029hl.bas"
OPEN "o", 4, "a029hh.bas"
FOR x = 1 TO 21 STEP 3
  INPUT #1, l, l2, l3
  INPUT #2, h, h2, h3
  avgl = (l + l2 + l3) / 3
  avgh = (h + h2 + h3) / 3
  WRITE #3, l, l2, l3, avgl
  WRITE #4, h, h2, h3, avgh
NEXT x
CLOSE #1
CLOSE #2
CLOSE #3
CLOSE #4
END
```

TABLE OF CONTENTS

## 1.0 Introduction

The Research Institute at the University of Alabama in Huntsville (UAH), was tasked by the Nondestructive Evaluation (NDE) Branch (EH-13) at Marshall Space Flight Center (MSFC) to conduct research in the method of electronic shearography for nondestructive evaluation. The goal of this research was to summarize and expand upon the existing theory describing electronic shearography.[1] It was desired that means of calibrating electronic shearography results be explored.

## 2.0 Background and Objectives:

The NDE Branch at MSFC maintains a laboratory for the application and development of the method of electronic shearography. This facility is equipped with a Pratt-Whitney Electronic Holography/Shearography Inspection System (PW EH/SIS) and Laser Technology, Inc. (LTI) SC-4000. Electronic shearographical techniques provide non-contact real-time location and sizing of defects in many material systems.

In addition to this type of qualitative analysis, electronic shearography is also capable of producing quantitative results. These results are in the form of fringe patterns in which each fringe is a contour of a constant change in a surface slope component. These fringe patterns are thus analogous to full field surface deformation values.

While the NDE Branch had successfully utilized electronic shearography for qualitative NDE, the branch lacked sufficient information to obtain deformation values from shearography results. The need was also identified to obtain adequate documentation to conveniently introduce the methodology of electronic shearography to those unfamiliar with the technique. The UAH Research Institute was contracted to fulfill these needs.

The objective of this task was to review existing literature on the theoretical description of electronic shearography and compile that information into a single document which could be used as an introduction to electronic shearography. This summary would also develop the existing theories into forms which could be used to obtain deformation measurements from fringe patterns. This process involves a calibration between fringe orders and surface slope components. This calibration was to be derived analytically and validated experimentally. Sources and magnitudes of calibration errors would also be discussed.

[1] A list of references is included.

## 3.0 Shearography Techniques:

Electronic shearography is a variation of traditional optical holography. That is, it is an optical technique which provides information about the imaged object in all three dimensions. Traditional optical holography provides a three dimensional image of the object by not only recording the spatial intensity distribution of the light reflected from the object but also the spatial phase distribution of the light reflected from the object. NDE application of holography allows the full field measurement of out of plane displacement ($w$), as illustrated in Figure 3.0, over the object surface as an interference fringe pattern produced by the superposition of two holograms at two different load states. However, this technique is very sensitive ($w < \lambda/4$) and usually requires that the apparatus and test object be extensively isolated from many environmental variations.

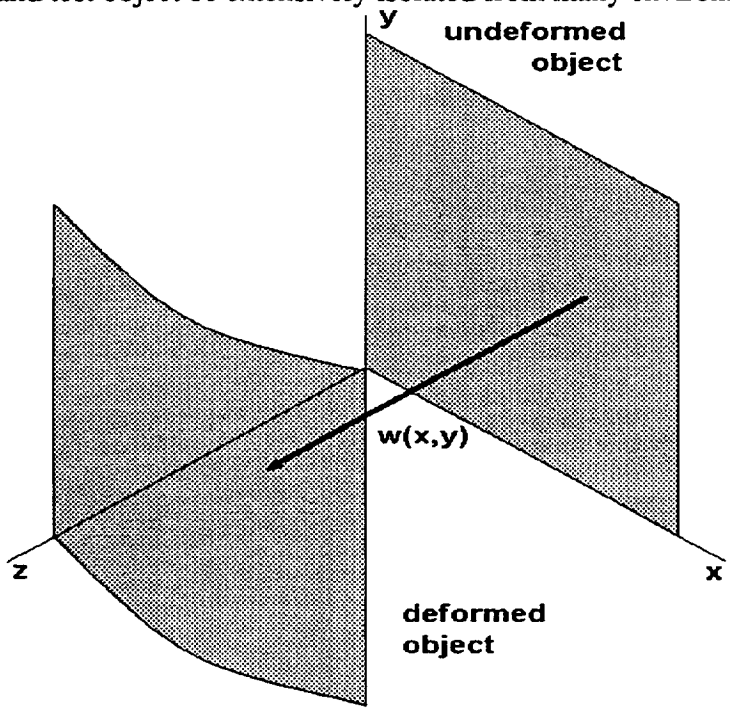


**Figure 3.0. Out of Plane Displacement Field**

Optical shearography differs from optical holography in that the image at each deformation state is actually the superposition of two images which are offset, or sheared, by some distance. The resulting interference fringes are related to components in the direction of image shearing of changes in the object surface slope ($\partial w/\partial x$). Electronic shearography utilizes a solid state video camera to record the shearograms rather than photographic film or plates. The use of electronic data acquisition provides shearographic results in real time. Electronic shearography is less sensitive than holography, and thus requires minimal isolation.

## 3.1 Basic Apparatus:

The components of a basic electronic shearography device are illustrated in Figure 3.1.1. An expanded beam from a coherent light source is used to illuminate the test object. The light reflected from the object passes through an image shearing lens arrangement before being recorded by the solid state video camera.

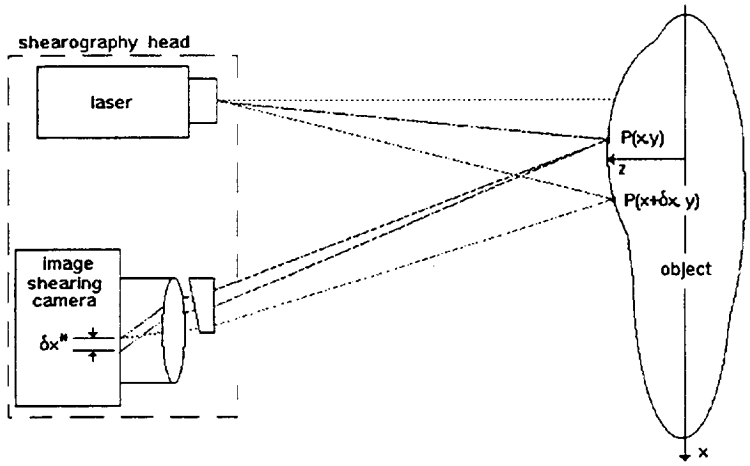


**Figure 3.1.1. Basic Electronic Shearography Device**

It is the effect of the image shearing lens that a point $P(x, y)$ on the object surface appears at two different points on the camera sensor grid, separated by some $\delta x^*$. This distance $\delta x^*$ characterizes the extent of the effect of the image shearing lens, but is not always convenient to measure. Another effect of the image shearing lens is that two points $P(x, y)$ and $P(x+\delta x, y)$ on the object surface appear at the same point on the image plane. The distance $\delta x$ also characterizes the degree of image shearing and may easily be measured on the object surface.

A change in the object surface slope over some small $\Delta x$ is illustrated in Figure 3.1.2. The light received by the camera from two points separated by $\Delta x$ will have two different phases due to the difference in the distance each ray has traveled from the source. If $\Delta x$ is equal to $\delta x$, then the light reflected by both points will be incident on the camera sensor grid at the same point. Interference from the two different phases will result in a fringe pattern shearogram indicating contours of $\partial w/\partial x$.

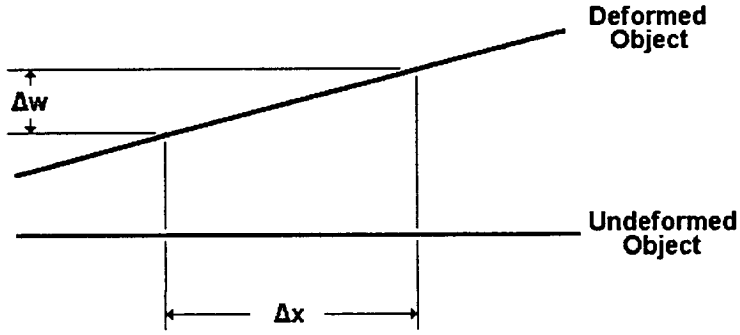

**Figure 3.1.2 Changes in Object Surface Slope Over Small Δx.**

The Laser Technology, Inc. (LTI) SC-4000 utilizes a varient of the basic shearography apparatus. A birefringent plate is used in place of the wedge shaped lens with the same results as shown in Figure 3.1.3. The shear distance is approximately 0.75 in. at an object distance of 8 ft. This system produces basic shearograms which are the superposition of a single undeformed and a single deformed image, each of which are the superposition of two sheared images at the same deformation state.

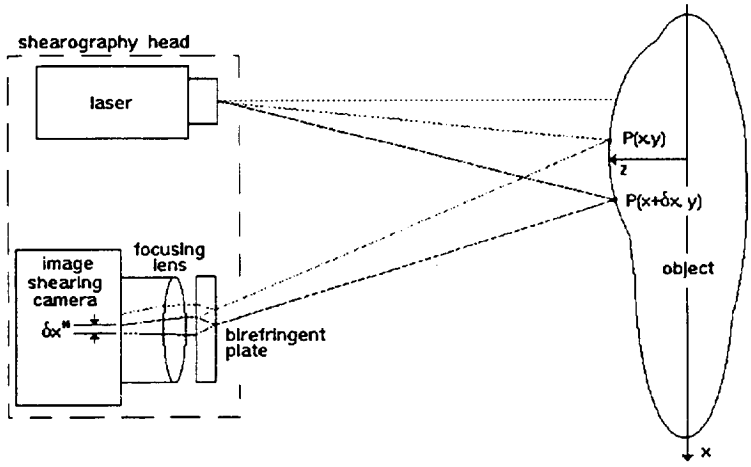


**Figure 3.1.3 LTI SC-4000 Shearography Device (Patent No. 4,887,899).**

## 3.2 Advanced Apparatus:

Modifications to the basic electronic shearography device allows greater flexibility in the type of evaluation conducted. The enhanced apparatus shown in Figure 3.2 is a typical alternative, which utilizes a modified Michelson interferometer in place of the image shearing wedge or birefringent plate. The Pratt-Whitney EH/SIS utilizes this optical arrangement. The image shearing mirror may be tilted and rotated to allow image shearing in any image plane direction by any shearing distance. This approach allows evaluation of a wider range of flaws. As the image shearing distance is adjusted, so is the number of fringes appearing for a given maximum slope. This advanced device also allows the production of sharper, clearer shearograms.

Objects in basic shearograms often appear to have irregular or "fuzzy" boundaries and surface features due to the random phase distribution of laser speckle illumination. Shearogram quality may be improved by employing frame averaging. Frame averaging acquires a series of images at each deformation state. The number of images acquired is user defined. The piezoelectric phase stepping mirror is positioned a different distance from the beam splitter for each image, and thus the zero-shear image for each frame is phase shifted from the others. The mean intensity of each pixel over the range of frames is used to produce a frame averaged image at each deformation stage. This function sharpens the features of the object surface and reduces noise in the resulting shearogram.

Basic shearograms also often appear "grainy", even after frame averaging, due again to the random phase distribution of laser speckle illumination. Speckle averaging in the PW EH/SIS employs a stepper motor driven etalon to rotate the illumination beam by 90° between image series. That is, a series of images is acquired at each beam rotation and averaged to produce the image at each deformation state. The total number of frames which are averaged to produce each image is thus four times the number of frames to be averaged. Speckle averaging produces sharper fringes and reduces noise. Speckle averaging may be used independent of frame averaging by setting the number of frames to average to 1 in the PW EH/SIS control software.

The Pratt-Whitney Electronic Holography/Shearography Inspection System utilizes the advanced shearography device described above. The PC based PW EH/SIS also allows the user to place labels and pointers on the image as graphics. A video caliper is provided which may be calibrated to real world coordinates and allows for the on-screen measurement of detection sizes.

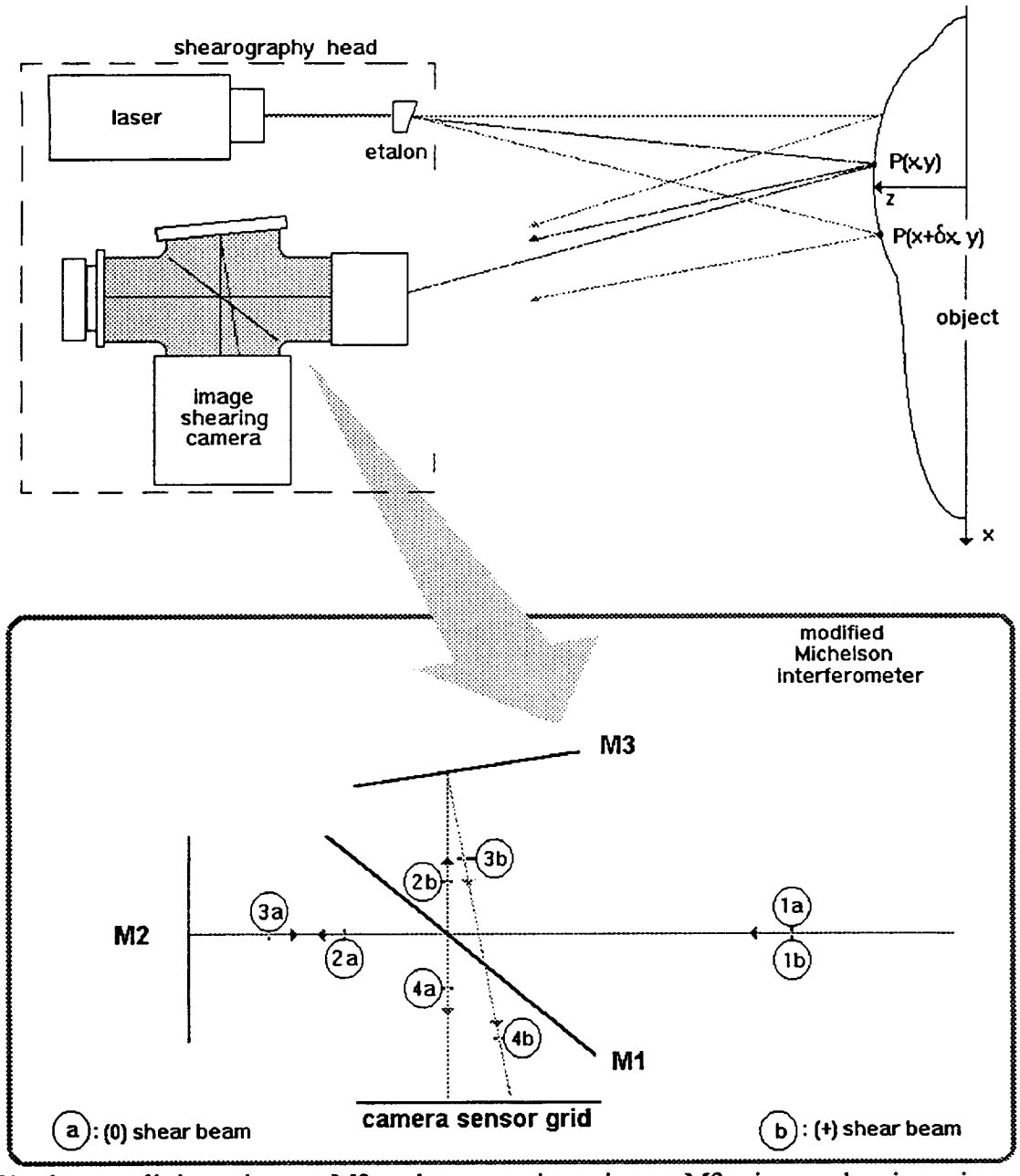


M1: beam splitting mirror M2: phase stepping mirror M3: image shearing mirror

1a: (0) shear beam reflected from object
2a: (0) shear beam passed through M1
3a: (0) shear beam reflected from M2
4a: (0) shear beam reflected from M1 toward camera

1b: (+) shear beam reflected from object
2b: (+) shear beam reflected from M1
3b: (+) shear beam reflected from M3
4b: (+) shear beam passed through M1 toward camera

**Figure 3.2. Advanced Shearography Device with Modified Michelson Interferometer (LTI Patent No. 5,094,528)**

## 4.0 Derivation of Theoretical Relationship Between Fringe-Order and Slope:

### 4.1 General Relationship:

For the undeformed (reference) image, the detected light intensity may be assumed to be of the form[3,4]:

$$I = I_o[1+\cos\phi] \qquad \text{<EQ.4.1.1>}$$

where $I_o$ = object surface spatial light intensity distribution,
and $\phi$ = random phase angle of light from source.

For the deformed image, the detected light intensity may be assumed to be of a similar form with a phase shift due to out of plane displacement of the object surface:

$$I' = I_o[1+\cos(\phi+\Delta)] \qquad \text{<EQ.4.1.2>}$$

where $\Delta$ = phase shift due to relative out of plane displacement between P(x,y) and P(x+δx,y) on the object surface,
and $\delta x$ = shear distance measured in object plane.

The shearogram is produced by superimposing the two images, or adding their intensities. Thus, from EQ.4.1.1 and EQ.4.1.2:

$$\begin{aligned} I_s &= I + I' = I_o[2+\cos\phi+\cos(\phi+\Delta)] \\ &= 2I_o + I_o[\cos\phi+\cos(\phi+\Delta)] \\ &= 2I_o + 2I_o(\tfrac{1}{2})[\cos\phi+\cos(\phi+\Delta)] \\ &= 2I_o[1+(\tfrac{1}{2})[\cos\phi+\cos(\phi+\Delta)]] \\ &= 2I_o[1+(\tfrac{1}{2})[\cos(\phi+\tfrac{\Delta}{2}-\tfrac{\Delta}{2})+\cos(\phi+\tfrac{\Delta}{2}+\tfrac{\Delta}{2})]] \\ &= 2I_o[1+(\tfrac{1}{2})[2\cos(\phi+\tfrac{\Delta}{2})\cos(\tfrac{\Delta}{2})]] \\ &= 2I_o[1+\cos(\phi+\tfrac{\Delta}{2})\cos(\tfrac{\Delta}{2})] \end{aligned}$$

$\therefore I_s = 2I_o$ if $\cos(\tfrac{\Delta}{2}) = 0$

$\Rightarrow \tfrac{\Delta}{2} = \tfrac{\pi}{2}(2N+1)$ where $N = \{0,1,2,3,\ldots\}$ are the fringe orders of the bright fringes.

$$\therefore \Delta = (2N+1)\pi \qquad \text{<EQ.4.1.3>}$$

Also, from geometry: $\Delta = \dfrac{2\pi}{\lambda}(A\delta u + B\delta v + C\delta w)$

where $A = \dfrac{x-x_0}{R_o} + \dfrac{x-x_s}{R_s}$, $B = \dfrac{y-y_0}{R_o} + \dfrac{y-y_s}{R_s}$, $C = \dfrac{z-z_0}{R_o} + \dfrac{z-z_s}{R_s}$

(where $z(x,y)$ = object surface,
$O(x_o, y_o, z_o)$ = camera position,
$S(x_s, y_s, z_s)$ = illumination source position,

$R_o^2 = x_o^2 + y_o^2 + z_o^2$, and
$R_s^2 = x_s^2 + y_s^2 + z_s^2$ )

$(u, v, w)$ = displacement vector of $P(x, y)$,

$(u+\delta u, v+\delta v, w+\delta w)$ = displacement vector of $P(x+\delta x, y)$, and

$\lambda$ = wavelength of illumination.

Assuming "small" $\delta x$: $\delta u \cong \frac{\partial u}{\partial x}\delta x,\ \delta v \cong \frac{\partial v}{\partial x}\delta x, \delta w \cong \frac{\partial w}{\partial x}\delta x$

$$\therefore \Delta = \frac{2\pi}{\lambda}\left(A\frac{\partial u}{\partial x} + B\frac{\partial v}{\partial x} + C\frac{\partial w}{\partial x}\right)\delta x \qquad \text{<EQ.4.1.4>}$$

Equating the expressions from EQ.4.1.3 and EQ.4.1.4:

$$\Delta = (2N+1)\pi = \frac{2\pi}{\lambda}\left(A\frac{\partial u}{\partial x} + B\frac{\partial v}{\partial x} + C\frac{\partial w}{\partial x}\right)\delta x$$

$$\therefore (2N+1)\frac{\lambda}{2\delta x} = A\frac{\partial u}{\partial x} + B\frac{\partial v}{\partial x} + C\frac{\partial w}{\partial x}$$

$$\therefore (N+\tfrac{1}{2})\frac{\lambda}{\delta x} = A\frac{\partial u}{\partial x} + B\frac{\partial v}{\partial x} + C\frac{\partial w}{\partial x}$$

where $n = \{0,1,2,3,...\} \approx (N + 1/2)$ are the fringe orders of the dark fringes.

$$\therefore \text{In general:}\quad \frac{n\lambda}{\delta x} = A\frac{\partial u}{\partial x} + B\frac{\partial v}{\partial x} + C\frac{\partial w}{\partial x} \qquad \text{<EQ.4.1.5>}$$

## 4.2 Special Cases:

### 4.2.1 Partial Laser/Camera Superpositioning:

If the illumination source position is in line with the optical axis of the camera, then $x_s = y_s = x_o = y_o = 0$. $\therefore R_o = z_o$ and $R_s = z_s$.

$$\therefore A = \left(\frac{1}{z_o} + \frac{1}{z_s}\right)x,\ B = \left(\frac{1}{z_o} + \frac{1}{z_s}\right)y,\ C = \left(\frac{z - z_o}{z_o} + \frac{z - z_s}{z_s}\right)$$

$\therefore$From EQ.4.1.5:

$$\frac{n\lambda}{\delta x} = \left(\frac{1}{z_o} + \frac{1}{z_s}\right)\left(x\frac{\partial u}{\partial x} + y\frac{\partial v}{\partial x}\right) + \left(\frac{z - z_o}{z_o} + \frac{z - z_s}{z_s}\right)\left(\frac{\partial w}{\partial x}\right)$$

$$\therefore \frac{n\lambda}{\delta x} = \left(\frac{1}{z_o} + \frac{1}{z_s}\right)\left(x\frac{\partial u}{\partial x} + y\frac{\partial v}{\partial x}\right) + \left[z\left(\frac{1}{z_o} + \frac{1}{z_s}\right) - 2\right]\left(\frac{\partial w}{\partial x}\right)$$

$$\therefore \frac{n\lambda}{\delta x} = \left(\frac{1}{z_o} + \frac{1}{z_s}\right)\left(x\frac{\partial u}{\partial x} + y\frac{\partial v}{\partial x} + z\frac{\partial w}{\partial x}\right) - 2\left(\frac{\partial w}{\partial x}\right) \qquad \text{<EQ.4.2.1>}$$

### 4.2.2 Total Laser/Camera Superpositioning:

If, in addition to the criterion for partial superpositioning of the laser and camera, the distance from the test object to the illumination source is the same as the distance to the camera, then $z_o = z_s = z^*$.

$\therefore$ From EQ.4.2.1

$$\frac{n\lambda}{\delta x} = \left(\frac{1}{z^*} + \frac{1}{z^*}\right)\left(x\frac{\partial u}{\partial x} + y\frac{\partial v}{\partial x} + z\frac{\partial w}{\partial x}\right) - 2\left(\frac{\partial w}{\partial x}\right)$$

$$\therefore \frac{n\lambda}{\delta x} = \left(\frac{2}{z^*}\right)\left(x\frac{\partial u}{\partial x} + y\frac{\partial v}{\partial x} + z\frac{\partial w}{\partial x}\right) - 2\left(\frac{\partial w}{\partial x}\right)$$

$$\therefore \frac{n\lambda}{\delta x} = \left(\frac{2}{z^*}\right)\left(x\frac{\partial u}{\partial x} + y\frac{\partial v}{\partial x} + z\frac{\partial w}{\partial x}\right) - \left(2\frac{z^*}{z^*}\right)\left(\frac{\partial w}{\partial x}\right)$$

$$\therefore n = \left(\frac{2\delta x}{\lambda z^*}\right)\left(x\frac{\partial u}{\partial x} + y\frac{\partial v}{\partial x} + (z - z^*)\frac{\partial w}{\partial x}\right) \qquad \text{<EQ.4.2.2>}$$

### 4.2.3 Approximately Ideal Laser/Camera Positioning:

If the distance from the shearography unit to the test object is much larger than the dimensions of the test object $\{x, y, z\}$ and the dimensions of the shearography unit $\{x_s, y_s, x_o, y_o\}$ then $x_s \cong x_o \cong y_s \cong y_o \cong 0$, and the case of 4.2.1 is approximated. Also $z_o \cong z_s \Rightarrow z^*$, andthe case of 4.2.2 is approximated. This results in:

$$\frac{x}{z^*} \cong \frac{y}{z^*} \cong \frac{z}{z^*} \cong 0.$$

$\therefore$ From EQ.4.2.2:

$$\frac{n\lambda}{2\delta x} \cong (0)\left(\frac{\partial u}{\partial x}\right) + (0)\left(\frac{\partial v}{\partial x}\right) + \left(0 - \frac{z^*}{z^*}\right)\frac{\partial w}{\partial x}$$

$$\therefore \frac{n\lambda}{2\delta x} \cong -\frac{\partial w}{\partial x}$$

$$\therefore \frac{\partial w}{\partial x} \cong -\frac{n\lambda}{2\delta x} \qquad \text{<EQ.4.2.3>}$$

#### 4.2.4 Actually Ideal Laser/Camera Positioning:

If the criteria are met for the special cases of 4.2.1, 4.2.2, and 4.2.3, then the approximate relation of EQ.4.2.3 becomes an equality.

$$\therefore \frac{\partial w}{\partial x} = -\frac{n\lambda}{2\delta x} \qquad \text{<EQ.4.2.4>}$$

## 5.0 Theoretical Shearographical Analysis of a Cantilever Beam:

### 5.1 General Derivations:

Figure 5.1 schematically illustrates a cantilever beam with a concentrated end load. The deflection of the beam *(w)* is given as a function of position along the beam *(x)* by:

$$w = \frac{P}{6EI_B}\left(3Lx^2 - x^3\right) \qquad \text{<EQ.5.1.1>}$$

Thus, the deflection at the end of the beam *($w_o$ = w(L))* may be expressed as:

$$w_o = \frac{PL^3}{3EI_B}$$

From which the load *(P)* may be expressed in terms of the end deflection:

$$P = 3\frac{EI_B}{L^3} w_o \qquad \text{<EQ.5.1.2>}$$

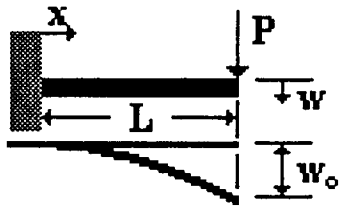


**Figure 5.1.** Cantilever Beam with Concentrated End Load

Substituting EQ.5.1.2 into EQ.5.1.1 gives the deflection along the beam in terms of the end deflection instead of the end load.

$$\therefore w = \frac{w_o}{2L^3}\left(3Lx^2 - x^3\right)$$

By differentiation:

$$\frac{\partial w}{\partial x} = \frac{w_o}{2L^3}\left(6Lx - 3x^2\right)$$

$$\therefore \frac{\partial w}{\partial x} = \frac{3w_o}{2L^3}\left(2Lx - x^2\right) \qquad \text{<EQ.5.1.3>}$$

Equating the expressions from EQ.4.2.4 and EQ.5.1.3, noting that $w$ is defined in opposite directions for beam theory and optical theory,

Equating the expressions from EQ.4.2.4 and EQ.5.1.3, noting that $w$ is defined in opposite directions for beam theory and optical theory,

$$\frac{\partial w}{\partial x} = \frac{n\lambda}{2\delta x} = \frac{3w_o}{2L^3}\left(2Lx - x^2\right)$$

$$\therefore n = 3\left(\frac{\delta x}{\lambda}\frac{w_o}{L^3}\right)\left(2Lx - x^2\right) \qquad \text{<EQ.5.1.4>}$$

EQ.5.1.4 predicts the dark fringe order at any position along the beam.

## 5.2 Particular Expressions

The Pratt Whitney EH/SIS and the LTI SC-4000 both use a green Niobium doped yttrium-aluminum-garnet (Nd:YAG) diode laser ($\lambda$ = 532 $\eta$m = 20.9E-6 in.). Thus, assuming $\delta x$ = 0.75 in., $\frac{\delta x}{\lambda} = 35885$. If $L$ = 10 in. and $w_o$ = 0.001 in., then $\frac{w_o}{L^3} = 1\times10^{-6}$.

$\therefore$From EQ.5.1.4: $$n = 0.1077\left(20x - x^2\right) \qquad \text{<EQ.5.2.1>}$$

This relationship is illustrated in Figure 5.2.

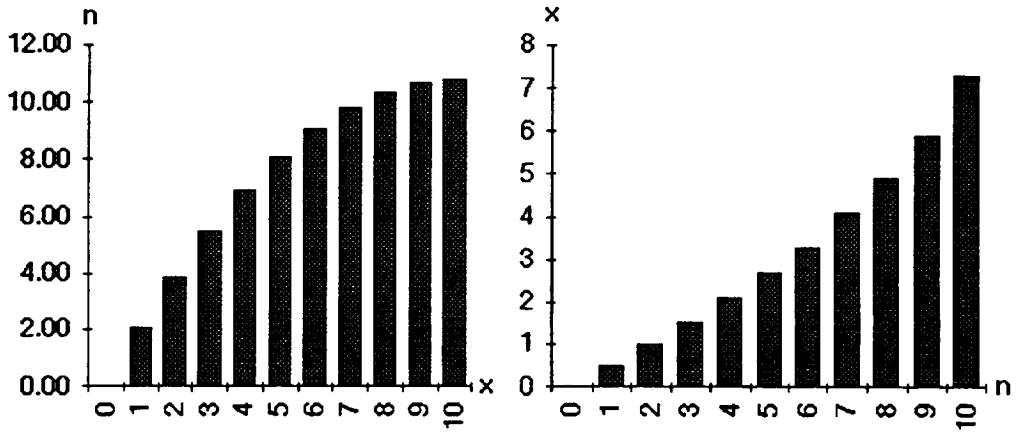


**Figure 5.2. Theoretical Relationship Between Fringe Order and Beam Position.**

## 6.0 Experimental Shearographical Analysis of a Cantilever Beam

An experiment was conducted with the PW EH/SIS electronic shearography system in which a cantilever beam was deflected at the free end by a micrometer. The variables in this experiment were given the same values as those assumed in the preceding theoretical analyses. The resulting shearogram is shown in Figure 6.0.1. on the next page.

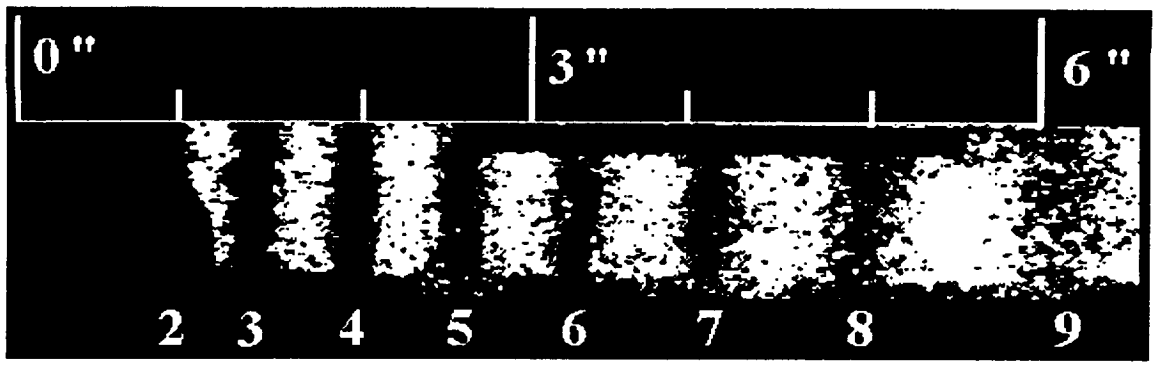


**Figure 6.0.1. PW EH/SIS Cantilever Beam Experiment**

The shearogram agrees very well with the theoretical predictions given above. For example, theory predicts dark fringe orders of $n = 9.0$ at $x = 6$ *in.* and $n = 5.5$ at $x=3$ *in.* The latter corresponds to a bright fringe order of $N = 5.0$ at $x=3$ *in* ($n \approx N+1/2$). The bright fringe $N = 5.0$ lies between the dark fringes $n = 5.0$ and $n = 6.0$. The relationship between the experimentally measured and theoretically predicted dark fringe positions is illustrated in Figures 6.0.3 and 6.0.4..

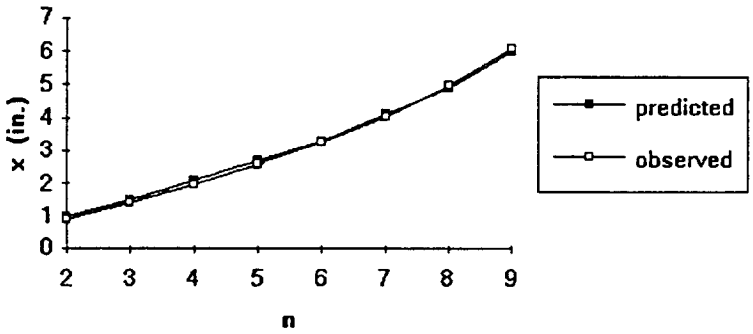


**Figure 6.0.3. Theoretical and Experimental Fringe Positions**

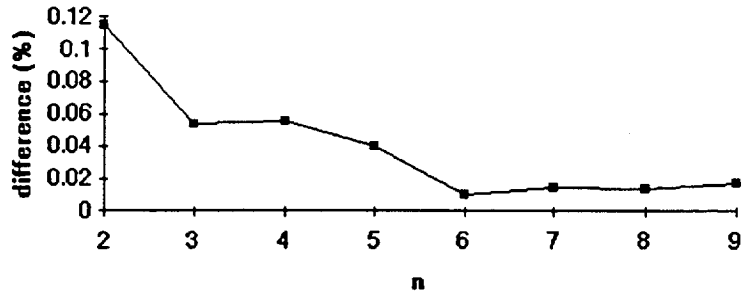


**Figure 6.0.4. Difference Between Theoretical and Experimental Fringe Positions**

## 7.0 Electronic Shearography Calibration with Cantilever Beams

The excellent correlation between the theoretical and experimental results for shearographic measurement of slope contours on cantilever beams suggest that such an experiment could be used to calibrate the fringe patterns obtained during shearographic NDE. For this purpose the relationship between the observed and predicted slopes provides calibration and error information.

The predicted slope of the beam at some position is given by EQ.5.1.3:

$$\frac{\partial w}{\partial x}=\frac{3w_o}{2L^3}(2Lx-x^2) \qquad \text{<EQ.7.1>}$$

The calibration equation, the observed slope of the beam at some fringe order, is given by EQ.4.2.4, noting the difference in direction of $w$,

$$\frac{\partial w}{\partial x}=\frac{n\lambda}{2\delta x} \qquad \text{<EQ.7.2>}$$

The observed percent relative error in this calibration is given by:

$$\xi_{opr}=\frac{\left(\frac{\partial w}{\partial x}\right)_{observed}-\left(\frac{\partial w}{\partial x}\right)_{predicted}}{\left(\frac{\partial w}{\partial x}\right)_{predicted}}\times 100\%$$

$$\therefore \xi_{opr}=\frac{\left(\frac{n\lambda}{2\delta x}\right)-\left(\frac{3w_o}{2L^3}\right)(2Lx-x^2)}{\left(\frac{3w_o}{2L^3}\right)(2Lx-x^2)}\times 100\%$$

$$\therefore \xi_{opr}=\left[\frac{\left(\frac{n\lambda}{2\delta x}\right)}{\left(\frac{3w_o}{2L^3}\right)(2Lx-x^2)}-1\right]\times 100\%$$

$$\therefore \xi_{opr}=\left[\left(\frac{L^3\lambda}{3w_o\delta x}\right)\left(\frac{n}{2Lx-x^2}\right)-1\right]\times 100\% \qquad \text{<EQ.7.3>}$$

This expression is evaluated by determining the position $x$ at which integer fringe orders $n$ occur on the calibration shearogram, then substituting into EQ.7.3 the $n$ and $x$ values corresponding to each fringe. Each fringe will have an associated observed percent

relative error. If the range of slopes to be encountered during subsequent testing is known or can be predicted, then the maximum error in those measurements may be taken as the maximum error observed in the expected range during calibration.

For the experiment conducted above, EQ.7.3 reduces to:

$$\xi_{opr} = \left[ (9.289)\left( \frac{n}{20x - x^2} \right) - 1 \right] \times 100\% \qquad \text{<EQ.7.4>}$$

This relationship is plotted in Figure 7.1; however, the error relationship for a given experiment is actually a curve and not a surface. EQ.5.2.1 must be applied as an additional restriction on $\xi_{opr}$. The result of substituting EQ.5.2.1 into EQ.7.4 is shown in Figure 7.2.

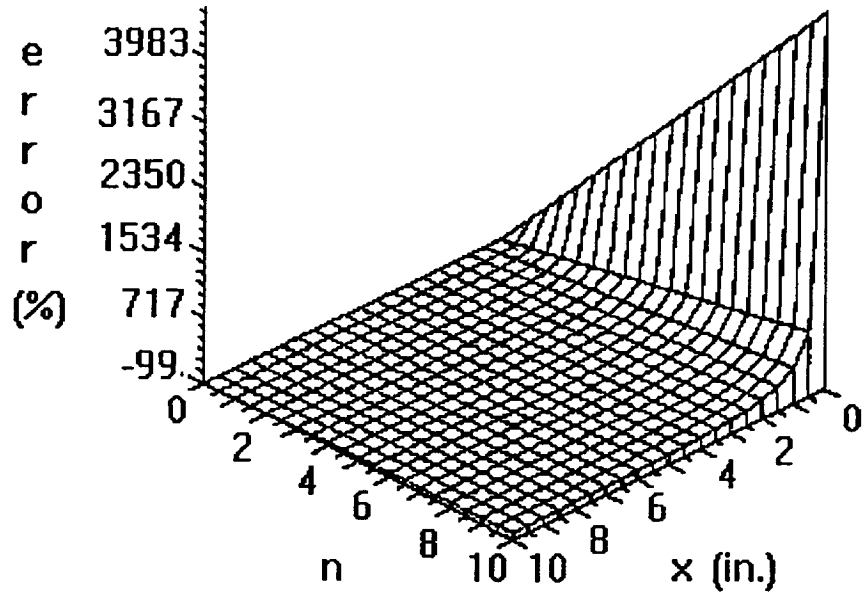


**Figure 7.1. Predicted Calibration Error as a Function of Fringe Order and Position**

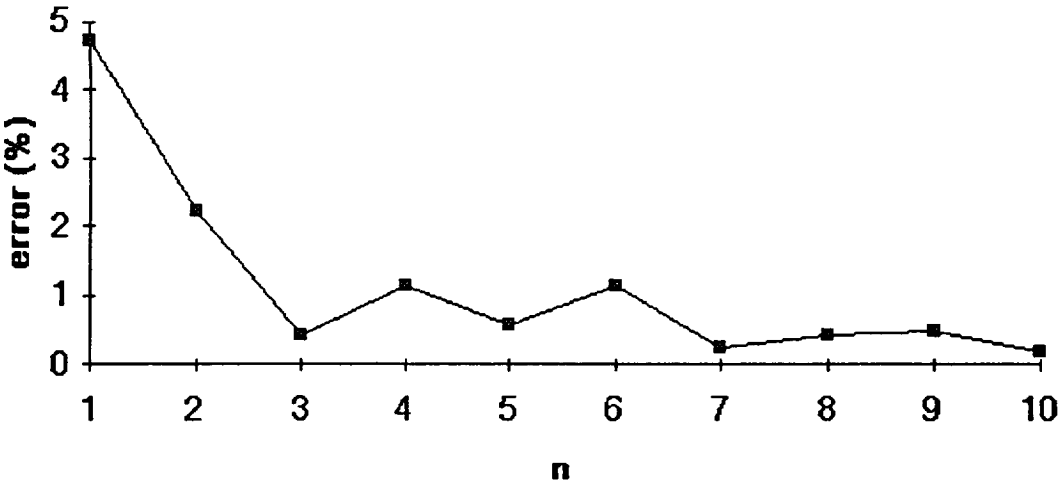


**Figure 7.2. Predicted Calibration Error as a Function of Fringe Order**

## 8.0 Conclusions

The general expression and several special cases of the relationship between surface deformation components and electronic shearography fringe orders have been derived. It has been shown that with ideal laser/camera positioning the surface slope components are directly proportional to the fringe orders. The constant of proportionality is negative one half of the ratio of the illumination wavelength to the shearing distance measured in the object plane.

It has also been shown that the theoretical analysis of a cantilever beam based on the ideal laser/camera positioning very closely matches experimental results from the Pratt-Whitney Electronic Holography/Shearography Inspection System and the Laser Technology Inc. SC-4000. The percent difference between the theoretical predictions and experimental measurements was observed to be much less than the observed percent relative calibration error. Thus the calibration error equation is a more conservative measure of the error associated with electronic shearography analysis. Furthermore, the calibration relationships and procedures developed herein may be utilized to determine full field values for changes in surface slopes from electronic shearography fringe patterns for more generalized geometries and loadings, providing a powereful tool for nondestructive evaluation and experimental mechanics.

## 9.0 REFERENCES


1. Boone, P.M., "Determination of Slope and Strain Contours by Double-exposure Shearing Interferometry", *Experimental Mechanics*, August 1975.

2. Engel, J.E., and Burleigh, D.D., "Validation of Laser Shearography Testing for Fixed Foam Insulation Bonds", *Review of Progress in Quantitative Nondestructive Evaluation*, Vol. 9, 1990.

3. Hung, Y.Y., "Shearography: A New Optical Method for Strain Measurement and Nondestructive Testing", *Optical Engineering*, May/June 1982.

4. Hung, Y.Y., "Shearography: A New Strain-Measurement Technique and a Practical Approach to Nondestructive Testing", *SEM Manual on Experimental Methods for Mechanical Testing of Composites*, 1989.

5. Laser Technology, Inc., *Advanced Shearography NDT*, 25 May 1994.

6. Maddux, G.A., Horton, C.M., Lansing, M.D., Gnacek, W.J., Newton, P.L., *Probability of Detection of Defects in Coatings with Electronic Shearography*, Technical Report 5-33267, University of Alabama in Huntsville-Research Institute, July 1994.

7. Mohanty, R.K., Joenathan, C., and Sirohi, R.S., "Speckle and Speckle-Shearing Interferometers Combined for the Simultaneous Determination of Out-of-plane Displacement and Slope", *Applied Optics*, 15 September 1985.

8. Mohanty, R.K., Joenathan, C., and Sirohi, R.S., "High Sensitivity Tilt Measurement by Speckle Shear Interferometry", *Applied Optics*, 15 May 1986.

9. Newman, John W., "Inspection of Aircraft Structure With Advanced Shearography", *1990 ASNT Fall Conference*, 10 October 1990.

10. Owner-Peterson, M., "Digital Speckle Pattern Shearing Interferometry: Limitations and Prospects", *Applied Optics*, 1 July, 1991.

11. Tay, C.J., Chau, F.S., Shang, H.M., Shim, V.P.W., and Toh, S.L., "The Measurement of Slope Using Shearography", *Optics and Lasers in Engineering*, 1990.

12. Toh, S.L, Shang, H.M., Chau, F.S., Tay, C.J., "Flaw Detection in Composites Using Time-Average Shearography", *Optics and Laser Technology*, Vol. 23, No. 1, 1991.

NASA
National Aeronautical and Space Agency

# Report Document Page

| 1. Report No. | 2. Government Accession No. | 3. Recipient's Catalog No. |
|---|---|---|
| | | |

**4. Title and Subtitle**

ACOUSTIC METHOD OF DAMAGE SENSING IN COMPOSITE MATERIALS

**5. Report Due**

**6. Performing Organization Code**

University of Alabama in Huntsville

**7. Author(s)**

Gary L. Workman

Matthew Lansing James Walker

**8. Performing Organization Report No.**

**10. Work Unit No.**

**9. Performing Organization Name and Address**

University of Alabama in Huntsville
Huntsville, Alabama 35899

**11. Contract or Grant No.**

**12. Sponsoring Agency Name and Address**

National Aeronautics and Space Administration
Washington, D.C. 20546-001
Marshall Space Flight Center, AL 35812

**13. Type of report and Period covered**

~~Quarterly~~ Final

**14. Sponsoring Agency Code**

MSFC

**15. Supplementary Notes**

**16.Abstract**

The use of acoustic emission and acousto-ultrasonics to characterize impact damge in composite structures is being performed on bothe graphite epoxy and kevlar bottles. Further development of the acoustic emission methodology to include neural net analysis and/or other multivariate techniques will enhance the capability of the technique to identify failure mechanisms during fracture. The acousto-ultrasonics technique will be investigated to determine it ability to predict regions prone to failure prior to the burst tests. The combination of the two methods will allow for simple nondestructive tests to be capable of predicting the performance of a composite structure prior to being placed in service and during service.

**17. Key Words (Suggested by Author(s))**

Acoustic Emission
Acoustic Ultrasonics
Nondestructive Testing, Composites
Damage Assessment

**18. Distribution Statement**

| | | |
|---|---|---|
| cc. | CN22D | (3) |
| | AT-01 | (1) |
| | EM-13/L. Smith | (1) |
| | ONRR | (1) |
| | Russell/EH-13 | (1 + reprol) |
| | Sci. & Tech. Inf. Fac. (1+ reprol) | |
| | Vaughan/UAH | (1) |

| 19. Security Class. (of this report) | 20. Security Class. (of this page) | 21. No. of pages | 22. Price |
|---|---|---|---|
| Unclassified | Unclassified | | |

NASA FORM 1626 OCT 86